NASA TECHNICAL NOTE

NASA TN D-8225

NASA TN D-8225

# AIRBORNE BALLISTIC CAMERA TRACKING SYSTEMS

*William L. Redish*

*Langley Research Center*
*Hampton, Va. 23665*

NATIONAL AERONAUTICS AND SPACE ADMINISTRATION • WASHINGTON, D. C. • JULY 1976

| 1 Report No | 2 Government Accession No | 3 Recipient's Catalog No |
|---|---|---|
| NASA TN D-8225 | | |

| 4 Title and Subtitle | 5 Report Date |
|---|---|
| AIRBORNE BALLISTIC CAMERA TRACKING SYSTEMS | July 1976 |
| | 6 Performing Organization Code |
| 7 Author(s) | 8 Performing Organization Report No |
| William L. Redish | L-10639 |
| | 10 Work Unit No |
| 9 Performing Organization Name and Address | 490-02-02-77 |
| NASA Langley Research Center | 11 Contract or Grant No |
| Hampton, Va. 23665 | |
| | 13 Type of Report and Period Covered |
| 12 Sponsoring Agency Name and Address | Technical Note |
| National Aeronautics and Space Administration | 14 Sponsoring Agency Code |
| Washington, D.C. 20546 | |

15 Supplementary Notes

16 Abstract

An operational airborne ballistic camera tracking system was tested for operational and data-reduction feasibility. This study discusses the acquisition and data processing requirements of the system. Suggestions for future improvements are also noted. A description of the data-reduction mathematics is outlined in the appendixes. Results from a successful reentry test mission have been tabulated. The test mission indicated that airborne ballistic camera tracking systems are feasible.

| 17 Key Words (Suggested by Author(s)) | 18 Distribution Statement |
|---|---|
| Optical tracking<br>Camera data processing<br>Airborne tracking<br>Reentry tracking | Unclassified – Unlimited<br><br>Subject Category 17 |

| 19 Security Classif (of this report) | 20 Security Classif (of this page) | 21 No of Pages | 22 Price* |
|---|---|---|---|
| Unclassified | Unclassified | 44 | $3.75 |

*For sale by the National Technical Information Service, Springfield, Virginia 22161

# AIRBORNE BALLISTIC CAMERA TRACKING SYSTEMS

William L. Redish
Langley Research Center

## SUMMARY

On April 27, 1968, Reentry-F mission, a turbulence heating experiment (ballistic reentry), provided the opportunity for an operational test of airborne ballistic camera tracking systems and methods. The use of postflight data to develop reduction techniques for this type of tracking mode was also made possible.

Two aircraft instrumented with ballistic cameras were flown as an independent tracking system during the mission. A well-established ground-based radar net was used for normal mission requirements and was assumed as the standard for the mission. The feasibility and overall accuracy of the airborne system were determined essentially by a direct comparison of data between the two systems.

This paper describes the data requirements and the special data-reduction techniques developed. A comparison study between the ground-based radar system and the airborne system is also presented.

## INTRODUCTION

Various orbital and reentry space tracking missions require tracking capabilities beyond the normal range of established land-based stations. These requirements indicate the importance of studying the feasibility of airborne or shipborne installations.

Aircraft installations have an advantage over land and ship networks because the aircraft can rise above local inclement weather. In operations where tracking areas may be changed prior to launch, aircraft installations offer the flexibility to accommodate these changes. The studies contained herein could affect the future planning and consideration of other types of airborne tracking systems such as radar-bearing aircraft used in conjunction with real-time star tracking devices.

Preliminary studies were undertaken at the National Aeronautics and Space Administration (NASA) Langley Research Center to determine the requirements for aircraft tracking stations using ballistic cameras. The feasibility of various data-reduction techniques was examined and checked by computer simulations. These studies indicated that mobile tracking stations presented special problems with regard to aircraft location,

camera orientation relative to the star field, and a moving baseline between the aircraft. Such problems had to be solved to compute the time-height profile of a reentry target vehicle with sufficient accuracy for the test mission requirements of a ±150-meter uncertainty.

The initial theoretical studies indicated that these problems could be minimized by the adaptation of special mathematical constraints. These constraints required specific measurements to be made aboard the airborne tracking stations. The required measurements onboard the aircraft are described in this paper. The data analysis procedures involving departures from standard fixed-camera methods are also described. The corresponding equations are discussed in the appendixes. These equations are outlined in general and are presented as guidelines for the future planning of similar missions.

The Reentry-F mission (ref. 1) provided the opportunity for a full operational test of the data-reduction techniques and equipment development. This mission, powered by the Scout launch vehicle S-164, boosted a payload into a ballistic reentry trajectory for spectra analysis of a special heat shield. Ground-based radar data furnished a reference for feasibility comparison with other tracking methods. The results of this comparison are presented in the figures.

## SYMBOLS

| | |
|---|---|
| A | azimuth angle, station coordinate system |
| $A_c, B_c, C_c$ | direction numbers of plane containing target and both tracking stations |
| $A_x, B_x, C_x$ | distortion coefficients, x-axis |
| $A_y, B_y, C_y$ | distortion coefficients, y-axis |
| B | magnitude of baseline between aircraft (See figs. 6(a) and 6(b).) |
| DE | difference between true zenith angle and refracted zenith angle |
| $D_j, D_k$ | distance between any camera-plate image j or image k and plate center measured within plane of plate (See fig. 11.) |
| $D_{jk}$ | distance between two camera-plate images j and k measured within plane of plate (See fig. 11.) |

| | |
|---|---|
| $D_{Tj}$ | distance between target image and star image j measured within plane of plate |
| E | elevation angle, station coordinate system |
| f | camera focal length (See fig. 11.) |
| GHA | Greenwich hour angle of Aries, west |
| h | geodetic height |
| $h_p$ | geodetic height of primary aircraft (See figs. 6(a) and 6(b).) |
| $h_s$ | geodetic height of secondary aircraft (See figs. 6(a) and 6(b).) |
| L | longitude, east |
| $_MC_2$ | number of statistical equations for M stars taken two at a time |
| $N_p$ | geodetic normal vector, primary aircraft (See figs. 6(a) and 6(b).) |
| $N_s$ | geodetic normal vector, secondary aircraft, after mathematical adjustment (See figs. 6(a) and 6(b).) |
| $N_s'$ | geodetic normal vector, secondary aircraft, based on navigator's position estimate (See figs. 6(a) and 6(b).) |
| P | primary aircraft position (See figs. 6(a) and 6(b).) |
| Q | computed target position (See figs. 6(a) and 6(b).) |
| $Q_c$ | fractional adjustment of surface refraction because of aircraft altitude |
| $\bar{R}$ | Earth radius at aircraft position (See fig. 10.) |
| $R_E$ | Earth equatorial radius |
| $R_j$ | star residual (radial displacement) |

| | |
|---|---|
| RM | mean star residual |
| $R_{xj}$ | star residual (x-axis component) |
| $R_{yj}$ | star residual (y-axis component) |
| r | distance from camera optical center to plate image |
| s | mathematically adjusted estimate of secondary aircraft position (See fig. 6(b).) |
| s' | navigator's estimate of secondary aircraft position (See fig. 6(a).) |
| $T_p$ | target line of sight from primary aircraft (See figs. 6(a) and 6(b).) |
| $T_s$ | target line of sight from secondary aircraft (See figs. 6(a) and 6(b).) |
| t | epoch time of observations |
| $t_g$ | time of Greenwich hour angle |
| $W_E$ | Earth rotation rate |
| $X_a, Y_a, Z_a$ | Cartesian coordinates of primary aircraft, sidereal system |
| $X_b, Y_b, Z_b$ | Cartesian coordinates of secondary aircraft, sidereal system |
| $X_j, Y_j$ | star residuals on x- and y-axes, respectively |
| $X_{mj}, Y_{mj}$ | measured plate coordinates, uncorrected for distortion |
| $X_p, Y_p$ | comparator axes |
| $X_{pc}, Y_{pc}$ | coordinates of focal point on camera plate |
| $X_{pj}, Y_{pj}$ | plate coordinates of star j, corrected for distortion |
| $X_{pk}, Y_{pk}$ | plate coordinates of star k, corrected for distortion |
| $X_T, Y_T$ | plate coordinates of target angle, corrected for distortion |

$Z$ zenith angle at station geodetic position, measured from geodetic normal vector

$Z_H$ scaled zenith angle to horizon at aircraft altitude (See fig. 10.)

$Z_p$ zenith angle of target vector from primary aircraft (See figs. 6(a) and 6(b).)

$Z_s$ zenith angle of target vector from secondary aircraft after mathematical adjustment (See fig. 6(b).)

$Z_s'$ zenith angle of target vector from secondary aircraft before mathematical adjustment (See fig. 6(a).)

$Z_{sc}$ scale zenith angle for adaptation of surface refraction to corresponding high altitude effects

$Z_t$ true zenith angle of star at station geodetic position

$\alpha_{jk}$ angle subtended by plate images with vertex at camera optical center

$\alpha_o$ altitude refraction coefficient

$\Delta H$ difference in horizon zenith angle between surface and high altitude (approximation)

$\epsilon$ Earth structural ellipticity

$\Gamma$ right ascension (sidereal longitude)

$\lambda, \mu, \nu$ direction cosines of vector relative to the $X, Y, Z$ axes, respectively, of a specified coordinate system

$\lambda_{pj}, \mu_{pj}, \nu_{pj}$ apparent direction cosines of control star $j$ in the sidereal system

$\phi$ geodetic latitude

Subscripts:

a primary aircraft

| | |
|---|---|
| app | designates apparent (refracted wave front of light) |
| b | secondary aircraft |
| c | aircraft subscript |
| j,k | star image designations |
| local | station coordinate system with vertex of axes at station position, X-axis pointed toward polar axis of Earth, Z-axis oriented along geodetic normal at station position, and Y-axis forming right-handed coordinate system |
| m | designates measured plate coordinates |
| sa | apparent star sidereal angle |
| sidereal | designates sidereal coordinate system, with X-axis pointing to first point of Aries |
| T | designates target plate image |
| x,y,z | designates specific coordinate axes for rotation of angles from one coordinate system to another coordinate system |

## AIRBORNE DATA ACQUISITION SYSTEM

The test mission operation used two aircraft: NASA 432 and NASA 438. Special instrumentation was installed on each aircraft. The instrumentation requirements are listed in figure 1.

Each aircraft contained a ballistic camera bolted to the aircraft viewport. Each camera had time-coded rotating shutters which produced an intermittent time-coded sequence of exposures of varying time durations. This system facilitated the time correlation between star-trail exposures and target-trail exposures on the individual camera plate.

The airborne system required one aircraft position to be known accurately. This knowledge was to be acquired through a loran C geodetic positioning system with a loran receiver installed on the primary aircraft. A multichannel recorder (MCTS) was mounted on each aircraft. This recorder produced the data tapes for subsequent use in the data analysis. (Data channels for respective aircraft are listed in fig. 1.)

On the primary aircraft, a radar system was adapted for the dual purposes of measuring the aircraft altitude and the magnitude of the instantaneous baseline between aircraft. The measurements were accomplished in an alternating sequence. On the secondary aircraft, a radar altimeter was installed for the purpose of measuring aircraft altitude. A timing mechanism system on each aircraft recorded the event times for the recorder channels on the respective aircraft. There was no time synchronization between aircraft.

Figures 1 and 2 illustrate the sequence of procedures from the data acquisition onboard the aircraft to the entry of data into the main computer data-reduction program. The auxiliary data sequences are shown in figure 1. The camera-plate analysis sequence of procedures is outlined in figure 2. After the mission, the tapes from the MCTS were processed through the data-reduction sequence noted in figure 1.

A separate computer program for the reduction of the loran C primary aircraft position data was obtained from the U.S. Coast Guard. Some minor modifications were made before the program was used with the mission data.

## AIRCRAFT FLIGHT MODE

Ground-station ballistic cameras are fixed to the surface of the Earth, and the star images record only the motion of the Earth relative to the star field. For short periods of time, the star trails are normally separate and distinguishable.

On the test mission, the ballistic cameras were bolted to the aircraft frame. Therefore, random aircraft motion could superimpose the separate camera exposures so that the individual time-coded exposures of the star trail could not be distinguished. During the short exposure time that occurs with reentry missions, it was sufficient to fly the aircraft in a gradual turning pattern. This pattern tended to spread these exposures across the camera plate so that each time exposure was normally separate and distinguishable. It is possible, however, that excessive aircraft roll, pitch, and yaw might interfere with this process by superimposing some of the chopped segments (overlapping one exposure segment on top of another). The merged exposures were ignored when reading the plate data.

For diffused targets such as those in the barium ion cloud experiment (refs. 2 and 3), this operational flight mode would not be practical because of the superimposition of image exposure of the cloud mass. This superimposition would cause erroneous densitometer readings on the cloud image, and thus prevent an accurate estimate of the mass center line.

## TARGET AND STAR FIELD COVERAGE

On the Reentry-F mission, the aircraft flew the turning pattern with the baseline essentially parallel to and south of the target track. Although the camera of each respective aircraft covered the respective targets for a longer period of time than is included in the subsequent data analysis, the simultaneous time overlap was approximately 2.35 seconds. The recorded time exposures for the two aircraft are presented in table I.

As a result of aircraft motion, some exposures were superimposed and could not be separated when the camera plates were analyzed. Consequently, the effective time overlap was reduced to approximately 1 second during which time the plates could be read accurately.

Plate 121224 (NASA 432) acquired 11 stars that were readable. Plate 121217 acquired only five stars of sufficient brightness to be read and identified accurately. Plate 121216 (NASA 432) was exposed by a separate camera but was not used in the computer reduction process. The following section discusses plate 121216 as it illustrates the effects of aircraft motion on plate readings.

## CAMERA-PLATE DATA DESCRIPTION

The effects of aircraft motion are noted in figure 3. A section of plate 121216 was selected and enlarged for this illustration. The camera shutters operated for a period of time prior to target acquisition. The small trace (star trail) illustrates the effects of aircraft motion on the resultant plate exposure during the total operating time of the camera. The eight target-trail exposures correspond to eight of the star-trail exposures (see fig. 3) and did not reflect appreciable aircraft motion during the short timespan of the target exposures in this specific enlargement.

Figure 3 also illustrates an exposure problem. An acceptable exposure for the star trail (small chops) resulted in an overexposure of the target trail (large chops). This overexposure caused considerable difficulty when reading the magnified image on the stereo comparator. Reasonable accuracy was obtained by reading the break points at the corners of the rectangular target chops to determine the beginning or ending of the chop. A mean between the two long sides of the rectangle was read for the center line of the target trail.

Plate 121216 (fig. 4) was selected to illustrate the effects of aircraft motion on the star plate readings. Interpolation between the fourth and fifth point on the graph could not be accomplished with the accuracy of the smooth curve segments on either side.

## TIME CORRELATION OF DATA

In the Reentry-F mission, the recorded data used were curve fitted and time interpolated before entering the computer reduction system. This procedure time-synchronized the data prior to the machine reduction process. The data were then entered in the computer program as if the time-code cycles of the camera shutters had been synchronized between the two aircraft during the mission. This method required extensive manual operation and greatly increased the operational time required for the reduction. Because of the experimental nature of the problem, this procedure was chosen for the following reasons:

(1) The overall complexity of the computer program was reduced so that all primary reduction procedures could be debugged and optimized.

(2) All input data were monitored manually for unexpected problems in the new prototype system.

(3) Machine curve fit error contributions were eliminated in the data output residuals during the development process.

## DATA ANALYSIS TECHNIQUES

A general outline of the mathematical techniques involved in the computer reduction program is given in appendixes A to H. The data-reduction sequence adapted for the airborne tracking system is illustrated in the flow diagram of figure 5. In figure 5, loop 2 and loop 3 control mathematical iteration cycles. Each camera plate was processed separately. Loop 1 represents the return for the second camera plate.

Astronomical star data for a specific epoch are compiled in star catalogs. The compiled star data must be updated to the tracking date and time. This procedure is briefly discussed in appendix A.

Since the camera plates were located within the atmosphere, the star images on the plates have been refracted. The astronomical direction cosines (true direction angles) must be transformed to refracted (apparent) direction cosines to be consistent with the observed plate data. The process used is described in appendix B.

Initially, the focal length and camera-plate center were not known accurately enough because of the unknown factors of lens and aircraft viewport distortion characteristics. These parameters must be solved for by a least-square matrix iteration process during the camera orientation. (See appendixes C and D.) During each iteration cycle (loop 3), the data editing and weighting procedures were also calculated. (See appendix E.)

After the residuals were minimized for the respective camera plate, the target angle for that plate was computed by the equations of appendix F. The entire process was then repeated using loop 1 for the second camera plate.

After the target angle for each plate was computed, the secondary aircraft was positioned with respect to the primary aircraft by the mathematical process described in appendix G. This geometric procedure is illustrated in figures 6(a) and 6(b) and is described as follows:

The position of the primary aircraft P was obtained by a loran C system. This position was assumed to be correct in the data-reduction process. An initial estimate of the secondary aircraft position s' was taken from the onboard navigator's data (fig. 6(a)). The adjusted secondary aircraft position s (fig. 6(b)) was subsequently determined by a mathematical process using the following data.

The magnitude of the baseline between the two stations B was measured by a radar-ranging system mounted on the aircraft. The respective geodetic heights $h_p$ and $h_s$ were determined by aircraft radar altimeters. The orientation of the target lines of sight $T_p$ and $T_s$ was determined by the ballistic cameras mounted on the viewports of each aircraft. This orientation used the star background for control points; the subsequent orientation angles were measured in the sidereal (star) coordinate system. The vectors $N_p$, $N_s$, and $N_s'$ represent geodetic normals to the theoretical ellipsoid of the Earth at the respective geodetic latitudes and longitudes of the respective stations. The angles $Z_p$, $Z_s$, and $Z_s'$ represent the zenith angles computed to estimate refraction corrections of star and target data.

In the reduction process, the initial estimated position of the secondary station s' was improved by forcing the target lines of sight $T_s$ and $T_p$ to intersect at Q while the measured range B and the altitudes $h_p$ and $h_s$ continued to be maintained. It should be noted that the target lines of sight $T_p$ and $T_s$ are rigidly determined by camera-plate reduction and that these lines of sight may be freely translated geometrically without changing their orientation. Therefore, when the initial secondary aircraft position s' is mathematically adjusted to a more correct position s the line $T_s$ is translated without changing its orientation. The two lines $T_s$ and the displacement are parallel because they represent the same orientation in the specified coordinate system. This process is repeated at each data point time epoch. After the secondary aircraft position was adjusted, the secondary aircraft camera plate was reprocessed through loop 2 of figure 5. The processing of the primary aircraft was negated after the first cycle of computations in loop 2. The final triangulation for target height and position was computed in the sequence as noted in figure 5. The selected process is described in appendix H.

## DATA ANALYSIS RESULTS

### Camera-Plate Processing

Ballistic camera plate 121224 produced 11 positively identified stars that were readable. The readable stars were adequately displaced over a sufficient plate area to facilitate distortion analysis. The iteration procedure for computing the distortion coefficient values reduced the mean star residual errors from 17.3 $\mu$m to 4.8 $\mu$m. This final value was close to the 2-$\mu$m value normally expected with ground-station fixed-camera systems.

Ballistic camera plate 121217 produced only five stars of sufficient magnitude to be read and identified. The small number of stars prevented distortion analysis for this plate. As a result, a statistical method based on successive approximations of the plate star residual errors was adapted to compensate partially for the camera and aircraft viewport distortion errors. The mean star residuals were improved from an initial 56.1 $\mu$m to a final 29.1 $\mu$m. The grouping of the stars on one side of this plate probably caused the higher initial mean star residual error as compared with the initial mean error of plate 121224.

### Triangulation Processing

Table II lists the results of the triangulation for the succeeding time epochs computed. The time-height profile graph for the payload target is shown in figure 7. The solid line represents the statistically smoothed ground radar track and was used as a basis of comparison. The circles represent airborne camera computed heights with no refraction corrections (minimum). The triangles represent the computed heights with surface refraction corrections (maximum). The final target computed heights with the assumed high altitude refraction corrections are represented by shaded diamonds and occur between the two computations shown. The height variation caused by the refraction uncertainty appears to be less than the 150-meter scale indicated on the graph.

Figures 8 and 9 illustrate the target position (latitude and longitude) relative to the computed position. The loran C equipment was operating at its maximum effective distance for reasonable accuracy. This distance probably resulted in the bias which offset the entire tracking net computed position as indicated on the graph. However, since the ranging system between aircraft maintained a continuous and accurate estimate of relative baseline distances, the time-height profile was not significantly affected.

## RECOMMENDATIONS FOR DATA IMPROVEMENTS

Although the feasibility of the airborne system time-height profile accuracy has been proven under marginal conditions, these conditions are not desirable for normal range operations. The marginal conditions are discussed in this section.

The aircraft viewport is a curved surface when viewed with the accuracy of a ballistic camera. During flight, the aircraft undergoes vibration and structural bending which cause variable window distortion and subsequent optical effects upon the entering wave front of light. A larger number of control stars well dispersed over the entire plate are needed for better resolution of these distortion effects. A minimum of 15 control stars is recommended to facilitate the editing and rejection of erroneous control-star data.

Three recommendations for acquiring a larger number of control stars are:

(1) Incorporate image intensification techniques to enhance the readability of dim stars without overexposing the target trail.

(2) Plan launch window constraints based on observable star field densities.

(3) Acquire camera-plate exposures over high star density areas during the aircraft approach to the mission tracking area.

The last suggestion would allow a reasonable distortion and refraction analysis in the event that the subsequent mission track covered a darker portion of the sky.

The use of time synchronization between camera shutters would tend to minimize the data-reduction process. This procedure would eliminate the necessity for adapting preliminary manual or machine data-interpolation procedures prior to the main reduction process.

## CONCLUDING REMARKS

An airborne ballistic camera tracking system was tested during a ballistic reentry space mission and was compared with a well-established ground-based tracking radar network. The experimental airborne system computed a time-height profile that compared favorably with the results from a ground-based radar system.

Airborne ballistic camera-plate data with an adequate number of recorded stars well dispersed across the entire plate may be reduced to a 5-$\mu$m plate accuracy. The final time-height target profile between the airborne system and the established ground system differed in altitude by less than 150 meters despite some marginal data.

Since this profile was within the limits initially set for the project, airborne tracking networks appear feasible. Some areas of necessary improvement to insure the accuracy of future missions are presented.

Langley Research Center
National Aeronautics and Space Administration
Hampton, Va. 23665
May 4, 1976

# APPENDIX A

## STAR DATA PROCESSING

The star data of the identified plate stars were obtained from a standard star catalog for the 1950 epoch (ref. 4). This information was updated to the mission time in the computer program.

First- and second-order polynomials were found to reproduce the star precession tables to the eighth significant figure. Since this calculation was adequate for a century of updating, these coefficients were built into the computer program. The nine precessional parameters were computed from these coefficients and were used in a rotational matrix to correct the star data. The star proper motion was also corrected to the current mission epoch.

## APPENDIX B

## REFRACTION CORRECTIONS

The corrected star angles (from appendix A) are true angles (within astronomical accuracy). Since the camera plates were exposed in the atmosphere, the plates actually record the refracted wave fronts of light. The star angles must be corrected for refraction before they can be used as orientation control points for a mission.

Since refraction is a local phenomenon in the vicinity of the tracking station, the Earth-centered sidereal star direction cosines must be rotated to a local coordinate system with the tracking station as the center of the system. The local system was defined with the x-axis pointing toward the north polar axis. The z-axis pointed along the local vertical, and the y-axis pointed west to form a right-handed coordinate system. The rotation is shown below in matrix form:

$$\begin{bmatrix} \lambda_{local} \\ \mu_{local} \\ \nu_{local} \end{bmatrix} = \begin{bmatrix} \lambda_x & \mu_x & \nu_x \\ \lambda_y & \mu_y & \nu_y \\ \lambda_z & \mu_z & \nu_z \end{bmatrix} \cdot \begin{bmatrix} \lambda_{sidereal} \\ \mu_{sidereal} \\ \nu_{sidereal} \end{bmatrix} \tag{B1}$$

The nine directional cosines $\lambda_x$ to $\nu_z$ are obtained from the best estimate of the station latitude and longitude. If the station position is adjusted during the reduction process, the apparent star angles should be recomputed before any further analysis is undertaken.

Geodetic longitude is changed to right ascension (sidereal longitude) by the relationship where

$$\Gamma = L + GHA + W_E(t - t_g) \tag{B2}$$

L station geodetic longitude, east

$\Gamma$ right ascension of geodetic normal

GHA Greenwich hour angle of Aries (from Air Almanac) measured west of Greenwich meridian

$W_E$ Earth rotation rate

$t$ time of current epoch

$t_g$ time of Greenwich hour angle, west

The nine rotational matrix elements are then computed from the foregoing declination and the right ascension of the geodetic normal as follows.

$$\lambda_x = -\sin \phi \cos \Gamma \tag{B3}$$

$$\mu_x = -\sin \phi \sin \Gamma \tag{B4}$$

$$\nu_x = \cos \phi \tag{B5}$$

$$\lambda_y = \sin \Gamma \tag{B6}$$

$$\mu_y = -\cos \Gamma \tag{B7}$$

$$\nu_y = 0 \tag{B8}$$

$$\lambda_z = \cos \phi \cos \Gamma \tag{B9}$$

$$\mu_z = \cos \phi \sin \Gamma \tag{B10}$$

$$\nu_z = \sin \phi \tag{B11}$$

The parameter $\phi$ is the declination of the geodetic normal (in this case, station geodetic latitude). The rotation into the local system is thus completed.

The true and the apparent direction cosines of the star vector of orientation may be expressed in terms of station azimuth A and elevation E. The azimuth is unchanged by refraction. The elevation angle (derived from the cofunction of the zenith angle measured from the geodetic normal) has both true and apparent relationships. These are:

$$\lambda_{local} = \cos E \cos A \tag{B12}$$

$$\mu_{local} = \cos E \sin A \tag{B13}$$

$$\nu_{local} = \sin E \tag{B14}$$

$$\lambda_{app} = \cos E_{app} \cos A \tag{B15}$$

$$\mu_{app} = \cos E_{app} \sin A \tag{B16}$$

$$\nu_{app} = \sin E_{app} \tag{B17}$$

where the subscript app denotes the apparent (refracted) angle.

The true elevation E and azimuth angles A were solved for in equations (B12) to (B14). The apparent elevation angle $E_{app}$ must be computed from E with some system of refraction corrections. The system used is described in the following paragraph.

The elevation angle E may be obtained from equation (B14) after the matrix rotation (eq. (B1)) is completed. The angle becomes

$$E = \text{arc sin } \nu_{local} \tag{B18}$$

The apparent direction cosine relationships are obtained by combining equations (B12) and (B15) and by combining equations (B13) and (B16) by the azimuth terms. Equation (B17) is unchanged:

$$\lambda_{app} = \frac{\cos E_{app}}{\cos E} \lambda_{local} \tag{B19}$$

$$\mu_{app} = \frac{\cos E_{app}}{\cos E} \mu_{local} \tag{B20}$$

$$\nu_{app} = \sin E_{app} \tag{B21}$$

An interim system based on a modification of reference 5 was adapted for the test mission. Additional information and techniques concerning high-altitude refraction may be obtained from references 6 to 8.

The surface refraction correction DE (ref. 5) is correlated with the apparent zenith angle $Z_{app}$ and the true zenith angle $Z_{sc}$ as shown:

$$DE = Z_{sc} - Z_{app} \tag{B22}$$

For higher altitudes, the value of DE decreases. This decreased value was modified by assuming an exponential scale gradient for a coefficient of DE. The scale gradient adapted is

$$Q_c = e^{-\alpha_o h} \tag{B23}$$

where $Q_c$ represents the fractional change of DE because of altitude h. When equation (B23) was adapted as a coefficient in equation (B22) and was rearranged, the first modification became

$$Z_{app} = Z_{sc} - Q_c(DE) \tag{B24}$$

The exponential coefficient $\alpha_o$ was experimentally determined by successive trial and error computations using plate 121224 with 11 stars. The accepted value was based on minimization of the mean star residuals on this plate.

A second modification was adapted and contributed to the minimization of the plate star residuals. The parameter DE (described in ref. 5) is based on a true zenith horizon angle of $90^o$ ($\pi/2$ radians). The parameter $Z_{sc}$ represents the true zenith angle $Z_t$ of the star. At the aircraft altitudes flown during the test mission, the zenith angle of the true horizon is slightly greater than $90^o$ (illustrated in fig. 10). The parameter $Z_{sc}$ then becomes a function of the true zenith angle $Z_t$. A proportional scale modification based on figure 10 was assumed. This modification is described in the next paragraph.

A local Earth radius $\bar{R}$ was computed for the specific aircraft position. From the geometry of figure 10, the maximum increase in zenith angle $\Delta H$ due to station altitude was approximated by the following geometric relationship:

$$\Delta H \approx \arccos\left(\frac{\bar{R}}{\bar{R} + h}\right) \tag{B25}$$

where h is the aircraft geodetic height. The increased horizon zenith angle $Z_H$ at the station altitude h is

$$Z_H = \frac{\pi}{2} + \arccos\left(\frac{\bar{R}}{\bar{R} + h}\right) \tag{B26}$$

The scale ratio is

$$\frac{Z_{sc}}{Z_t} = \frac{\frac{\pi}{2}}{Z_H} \tag{B27}$$

When equation (B26) is substituted into equation (B27) by $Z_H$ and the result is substituted into equation (B24) by $Z_{sc}$, the apparent zenith angle becomes

$$Z_{app} = \frac{\frac{\pi}{2}(Z_t)}{\frac{\pi}{2} + \left[\arccos\left(\frac{\bar{R}}{\bar{R} + h}\right)\right]} - Q_c(DE) \tag{B28}$$

If the zenith angles $Z_t$ and $Z_{app}$ of equation (B28) are expressed in terms of their corresponding elevation angles $E$ and $E_{app}$:

$$Z_t = \frac{\pi}{2} - E \tag{B29}$$

and

$$Z_{app} = \frac{\pi}{2} - E_{app} \tag{B30}$$

the relationship becomes

$$E_{app} = \frac{\frac{\pi}{2}(\Delta H + E)}{\frac{\pi}{2} + \Delta H} + Q_c(DE) \tag{B31}$$

The parameters $Q_c$ and $\Delta H$ are the relationships expressed by equations (B23) and (B25), respectively. Equation (B31) may be substituted into equations (B19) to (B21) to compute the apparent direction cosines $\lambda_{app}$, $\mu_{app}$, and $\nu_{app}$.

These apparent star angles may then be rotated back to the sidereal system by an inverse matrix rotation as shown:

$$\begin{bmatrix} \lambda_{sa} \\ \mu_{sa} \\ \nu_{sa} \end{bmatrix} = \begin{bmatrix} \lambda_x & \lambda_y & \lambda_z \\ \mu_x & \mu_y & \mu_z \\ \nu_x & \nu_y & \nu_z \end{bmatrix} \begin{bmatrix} \lambda_{app} \\ \mu_{app} \\ \nu_{app} \end{bmatrix} \tag{B32}$$

$$\tag{B33}$$

$$\tag{B34}$$

The subscript $sa$ designates the apparent star sidereal angle exposed on the ballistic camera plates. These final direction cosines were then used in the following procedures.

## APPENDIX C

## CAMERA ORIENTATION EQUATIONS

In previous operations, fixed-camera systems have usually been oriented to a geodetic system involving a rigidly surveyed local vertical. The interior camera geometry and the star field were related to the local vertical by initially using the best estimate of the station position and solving for the following parameters in a least-square matrix iteration.

(1) Focal length of camera;

(2) Plate center (intersection of the camera focal line with the plane of the exposed plate or film) in the plate coordinate system;

(3) Camera tilt angle about the focal line;

(4) Right ascension and declination (or azimuth and elevation) of the focal line vector.

Aircraft motion and the complexity of stabilized platforms indicated that a new method which excluded the local vertical was needed. It was noted that the star field (projected upon the camera plate) constituted a unique set of geometric interrelationships when projected through the camera geometry. Relative star displacements on the exposed camera plates (or film) represented relative angular displacements of the stars projected onto a celestial sphere. Although the exposure was made near the surface of the Earth, these angles are essentially equal to those measured from the center of the Earth because of the absence of measurable star parallax. Because of this similarity, the measured displacement angle between two specific stars is essentially constant from any point in the solar system and, therefore, independent of any planetary geodetic coordinate system. This criterion indicated that a basic cosine equation was adequate to describe the relative displacement angles of points on the plate.

The basic equation also excluded the necessity of solving for the pointing angle of the focal line vector and the camera tilt angle. Three variables were thus eliminated from the least-square matrix solutions, and a rapid convergence for the three remaining unknowns was insured. This equation and its related forms are described in the following paragraphs.

The following general cosine equation is based on the inverted coordinates of the camera geometry of figure 11. This equation is used statistically to combine star pairs $j$ and $k$ over all available stars on the plate to minimize the residual errors of star images. The basic relationship is

$$D_{jk}^2 = r_j^2 + r_k^2 - 2r_j r_k \cos \alpha_{jk} \tag{C1}$$

where

$D_{jk}$ plate distance between plate star images

r distance from camera optical center to a respective subscripted star image j or k on plate

The angle $\alpha_{jk}$ with the vertex at the camera optical center is obtained by the dot product of any two subtending vectors with orientation $\lambda$, $\mu$, and $\nu$ through corresponding images on the plate. The equation is given as follows:

$$\cos \alpha_{jk} = \lambda_j \lambda_k + \mu_j \mu_k + \nu_j \nu_k \tag{C2}$$

The parameters $r_j$ and $r_k$ represent the vector magnitude from the camera optical center to the respective plate images. These parameters relate to the focal length f and force the focal line vector to remain essentially perpendicular to the plate by the following relationships:

$$r_j^2 = f^2 + D_j^2 \tag{C3}$$

$$r_k^2 = f^2 + D_k^2 \tag{C4}$$

where

f camera focal length

D distance from focal point on plate to respective subscripted star image on plate

The distances (in the plane of the plate, between plate images) are computed from the following parameters:

$X_{pj}, Y_{pj}$ arbitrary plate coordinates of star image j corrected for distortion

$X_{pk}, Y_{pk}$ arbitrary plate coordinates of star image k corrected for distortion

$X_{pc}, Y_{pc}$ arbitrary plate coordinates of focal point on plate

## APPENDIX C

The arbitrary plate coordinate system essentially constitutes the axes of the stereocomparator plate or film reader. Since the basic cosine equation expresses the displacement differences, the actual location of the comparator axes $X_p$ and $Y_p$ is immaterial.

In figure 11, the distances (normally corrected for distortion) between plate images are expressed as

$$D_j^2 = \left(X_{pj} - X_{pc}\right)^2 + \left(Y_{pj} - Y_{pc}\right)^2 \tag{C5}$$

$$D_k^2 = \left(X_{pk} - X_{pc}\right)^2 + \left(Y_{pk} - Y_{pc}\right)^2 \tag{C6}$$

$$D_{jk}^2 = \left(X_{pk} - X_{pj}\right)^2 + \left(Y_{pk} - Y_{pj}\right)^2 \tag{C7}$$

When equations (C5) and (C6) are substituted into equations (C3) and (C4), respectively, the following equations are obtained:

$$r_j^2 = f^2 + \left(X_{pj} - X_{pc}\right)^2 + \left(Y_{pj} - Y_{pc}\right)^2 \tag{C8}$$

$$r_k^2 = f^2 + \left(X_{pk} - X_{pc}\right)^2 + \left(Y_{pk} - Y_{pc}\right)^2 \tag{C9}$$

The final equation results when the relationships of equations (C2), (C7), (C8), and (C9) are substituted into equation (C1). This equation becomes

$$\left(X_{pk} - X_{pj}\right)^2 + \left(Y_{pk} - Y_{pj}\right)^2 = 2f^2 + \left(X_{pj} - X_{pc}\right)^2 + \left(Y_{pj} - Y_{pc}\right)^2 + \left(X_{pk} - X_{pc}\right)^2 + \left(Y_{pk} - Y_{pc}\right)^2 - 2\sqrt{\left(f^2 + D_j^2\right)\left(f^2 + D_k^2\right)}\left(\lambda_j\lambda_k + \mu_j\mu_k + \nu_j\nu_k\right) \tag{C10}$$

where $D_j$ and $D_k$ are obtained from equations (C5) and (C6), respectively.

The parameters $X_{pj}$, $Y_{pj}$, $X_{pk}$, and $Y_{pk}$ represent the plate image coordinates after statistical correction for distortion. The relationship between the corrected coordinates and the actual plate measurements is discussed in appendix D.

The combinations of star pairs produce a maximum statistical use of the star data available. For $M$ stars taken two at a time, the number of statistical equations available are

$${}_MC_2 = \frac{M!}{2(M-2)!} \tag{C11}$$

Therefore, for the five-star plate 121217 there are 10 statistical equations. The number of equations probably explains the statistical improvement of the accuracy of this plate as noted in the section "Data Analysis Results."

## APPENDIX D

## DISTORTION COEFFICIENT FORMS

Numerical analyses indicated that for the Reentry-F mission, the distortion characteristics of the camera lens and aircraft viewport approximated a sine wave function on each axis. The subsequent relationships between the corrected plate image coordinates and the measured image coordinates follow:

$$X_{pj} = A_x \sin\left[B_x\left(X_{mj} - X_{pc}\right) - B_x C_x\right] + X_{mj} \tag{D1}$$

$$Y_{pj} = A_y \sin\left[B_y\left(Y_{mj} - Y_{pc}\right) - B_y C_y\right] + Y_{mj} \tag{D2}$$

where

$X_{pj}, Y_{pj}$ plate star image coordinates statistically corrected for distortion

$X_{mj}, Y_{mj}$ measured plate star image coordinates

$A_x, B_x, C_x$ distortion coefficients, x-axis

$A_y, B_y, C_y$ distortion coefficients, y-axis

j star images j or k

If equations (D1) and (D2) are substituted into equation (C10), a final equation is obtained for each star pair processed. The unknowns f, $X_{pc}$, $Y_{pc}$, $A_x$, $B_x$, $C_x$, $A_y$, $B_y$, and $C_y$ may then be solved over all available stars by a matrix iteration least-square process. The resulting plate residuals may then be computed directly from equations (D1) and (D2) as shown:

$$\text{Residual}\left(X_j\right) = X_{pj} - X_{mj} \tag{D3}$$

$$\text{Residual}\left(Y_j\right) = Y_{pj} - Y_{mj} \tag{D4}$$

The parameters $X_{pj}$ and $Y_{pj}$ represent the computed plate coordinates for star j, statistically corrected for distortion. The statistical mean residual over all stars was used as a criterion for determining the feasibility of the plate data-reduction processes.

## APPENDIX E

## DATA EDITING AND WEIGHTING PROCESS

In the test mission, the star field for a specific plate presented the only control available for computing the related camera orientation. Erroneous control star data could conceivably have a significant effect on the final accuracy of the system. A relative weighting process was therefore adapted for the purpose of down weighting inconsistent star data within the field of view of each camera plate.

The weighting process was based on the final residuals of equations (D3) and (D4) after the best estimates of the distortion coefficients were obtained. The computed weights for each available control star were used in the subsequent iterations (to loop 3, fig. 5) for statistically improved values of focal length, plate center location, and distortion coefficients.

A Gaussian distribution form was adapted for this process. The radial displacement residual of each star was computed as shown:

$$R_j = \sqrt{R_{xj}^2 + R_{yj}^2} \tag{E1}$$

where

$R_{xj}$ residual $X_j$

$R_{yj}$ residual $Y_j$

as noted in equations (D3) and (D4). A statistical mean residual (RM) over all available stars on the plate was computed. The resultant weight was computed for each control star j by the following relationship:

$$\text{Weight (j)} = \frac{1}{e^{\left|\frac{R_j}{RM}\right|^2}} \tag{E2}$$

These weights were subsequently changed for each iteration cycle of loop 3 (fig. 5). When the plate residuals were minimized through the overall iteration process, the final data were used for the computation of the target angle.

## APPENDIX F

## TARGET ANGLE REDUCTION

After the best statistical estimates of the focal length, plate center, and distortion coefficients have been computed, any direction cosine of a target image on the plate may be computed by rearranging equations (C1) and (C2) as shown:

$$\lambda_j(\lambda_T) + \mu_j(\mu_T) + \nu_j(\nu_T) = \frac{r_T^2 + r_j^2 - D_{Tj}}{2r_T r_j} \tag{F1}$$

where

$$r_T^2 = f^2 + \left(X_T - X_{pc}\right)^2 + \left(Y_T - Y_{pc}\right)^2 \tag{F2}$$

$$r_j^2 = f^2 + \left(X_{pj} - X_{pc}\right)^2 + \left(Y_{pj} - Y_{pc}\right)^2 \tag{F3}$$

$$D_{Tj} = \left(X_T - X_{pj}\right)^2 + \left(Y_T - Y_{pj}\right)^2 \tag{F4}$$

and

$X_T, Y_T$ plate target coordinates, corrected for distortion

$X_{pj}, Y_{pj}$ plate star coordinates, corrected for distortion

$X_{pc}, Y_{pc}$ coordinates of focal point on plate

$f$ focal length of camera

$\lambda_T, \mu_T, \nu_T$ apparent direction cosines of target image in sidereal system

$\lambda_{pj}, \mu_{pj}, \nu_{pj}$ apparent direction cosines of control star in sidereal system

This process produces one equation for each control star j. The target angles are unknown and may be solved for over all usable stars on the plate in a least-square sense. The resultant direction cosines $\lambda_T$, $\mu_T$, and $\nu_T$ are then corrected for refraction and subsequently used for adjusting the secondary aircraft position and computing the final triangulation position as described in appendixes G and H.

## APPENDIX G

## RELATIVE POSITIONING WITHIN THE AIRCRAFT NET

The relative positions of the aircraft within the net were determined in the actual data-reduction process. The process is illustrated in figures 6(a) and 6(b). The aircraft positions were measured in the geodetic coordinate system based on the Greenwich meridian. The orientation of the target lines of sight $T_p$ and $T_s$ were reduced in the sidereal coordinate system. Coordinate rotations were made from the geodetic to the sidereal system for compatibility of data.

The target line of sight $T_s$ was translated mathematically until it intersected with line of sight $T_p$ at point Q. Point Q is essentially correct when the measured distance B and the measured height $h_s$ are maintained during the translation process. The position s then represents the corrected relative position of the secondary aircraft, and the subsequent triangulation was based on this position.

It should be noted that this method precludes residual analyses from the resultant triangulation. In this case, triangulation residuals merely indicate the mathematical accuracy of the entire boundary solution process. Consequently, a mission comparison with a well-established ground-based tracking net was necessary to establish an estimate of the overall accuracy of the system.

The mathematical adjustment is accomplished by the combination of the three nonlinear constraints into a 2 by 2 determinant. The three constraints are described as follows:

The first constraint concerns the primary aircraft position with subscript a and the measured range B to the secondary aircraft position with subscript b. This process is mathematically described by a sphere of radius B with the center at the primary geodetic position:

$$B^2 = \left(X_b - X_a\right)^2 + \left(Y_b - Y_a\right)^2 + \left(Z_b - Z_a\right)^2 \tag{G1}$$

Theoretically, the two stations and the target point lie in the same plane when the secondary position is adjusted and the target lines of sight are forced to intersect at any time epoch condition. This instantaneous epoch plane (from ref. 9) can be expressed in linear mathematical form by

$$\left(X_b - X_a\right)A_c + \left(Y_b - Y_a\right)B_c + \left(Z_b - Z_a\right)C_c = 0 \tag{G2}$$

where

$$A_c = \mu_b \nu_a - \nu_a \mu_b \tag{G3}$$

$$B_c = \lambda_a \nu_b - \lambda_b \nu_a \tag{G4}$$

$$C_c = \lambda_b \mu_a - \lambda_a \mu_b \tag{G5}$$

and $\lambda$, $\mu$, and $\nu$ represent the target direction cosines of the respective aircraft. The respective direction cosines $\lambda$, $\mu$, and $\nu$ are the true (unrefracted) target directional cosines.

The third constraint is expressed in Cartesian parametric form. These relationships contain the geodetic relationships required and are described as follows:

$$K_E = \frac{R_E}{\sqrt{1 - \epsilon^2 \sin^2 \phi}} \tag{G6}$$

$$X_c = \left(h_c + K_E\right) \cos \phi \cos \Gamma \tag{G7}$$

$$Y_c = \left(h_c + K_E\right) \cos \phi \sin \Gamma \tag{G8}$$

$$Z_c = \left[h_c + \left(1 - \epsilon^2\right) K_E\right] \sin \phi \tag{G9}$$

where

| | |
|---|---|
| h | geodetic height of station above ellipsoid of Earth |
| $\epsilon$ | structural ellipticity of ellipsoid of Earth |
| $R_E$ | structural equatorial radius of ellipsoid of Earth |
| $\Gamma$ | right ascension of station position |
| c | aircraft subscript a or b |

The right ascension $\Gamma$ is obtained from the relationship in equation (B2). If equations (G7), (G8), and (G9) are substituted into the constraint equations (G1) and (G2) by the appropriately subscripted X, Y, and Z, two equations in two unknowns are available. The two unknowns are the latitude $\phi$ and the longitude L of the secondary station.

## APPENDIX G

When the two resultant nonlinear equations were linearized by Taylor's Series and formed into a 2 by 2 determinant, they were found to be highly convergent with five to seven iterations. The initial trial values for the iteration were not critical.

This adjustment changed the orientation of the station geodetic normal from $N'_S$ of figure 6(a) to $N_S$ of figure 6(b). This process changes the zenith angle $Z'_S$ to zenith angle $Z_S$; subsequently, the resultant refraction correction for the camera plates of the secondary station is changed. The change in refraction was between 1 and 2 percent of its prior value. Although this change is small, the entire plate reduction process was recomputed to obtain the maximum possible accuracy from the system. This adjustment completed the final data required for the resultant triangulation for target position and output parameters as described in appendix H.

## APPENDIX H

## TRIANGULATION

After the secondary aircraft position was adjusted, the final target height and position were computed. The process selected was based on the geometric iteration illustrated in figure 12.

The iteration procedure is initially started from the position of the primary station. A line was projected from point p to point A and perpendicular to the fixed line of sight $T_s$. Another perpendicular was dropped from A to K. The iteration was continued until the minimum distance between $T_p$ and $T_s$ was obtained. This minimum distance determined the convergence criterion. The final target point is assumed half-way between the two lines of sight along this minimum perpendicular distance if any error of intersection remains. In the mobile tracking net, when the lines of sight are forced to intersect, no triangulation error can be determined. In fixed-station tracking nets, this minimum distance would represent a triangulation residual since the lines of sight are not forced to intersect by the adjustment procedure used in airborne systems.

## REFERENCES


1. Rumsey, Charles B.; Carter, Howard S.; Hastings, Earl C., Jr.; Raper, James L.; and Zoby, Ernest V.: Initial Results From Flight Measurements of Turbulent Heat Transfer and Boundary-Layer Transition at Local Mach Numbers Near 15 (Reentry F). NASA TM X-1856, 1969.

2. Fricke, Clifford L.: Triangulation of Multistation Camera Data To Locate a Curved Line in Space. NASA TN D-7538, 1974.

3. Adamson, David; Fricke, Clifford L.; and Long, Sheila Ann T.: Results of Magnetospheric Barium Ion Cloud Experiment of 1971. NASA TR R-437, 1975.

4. Staff Smithsonian Astrophysical Observatory: Star Catalog. Positions and Proper Motions of 258,997 Stars for the Epoch and Equinox of 1950.0. Publ. 4652, Smithsonian Institution, 1966. Part 1: Stars 000 001-073 708 (Bands $+80^{\circ}$ to $+30^{\circ}$). Part 2: Stars 073 709-128 547 (Bands $+20^{\circ}$ to $+0^{\circ}$). Part 3: Stars 128 548-192 333 (Bands $-0^{\circ}$ to $-20^{\circ}$). Part 4: Stars 192 334-258 997 (Bands $-30^{\circ}$ to $-80^{\circ}$).

5. Brown, Duane C.: A Treatment of Analytical Photogrammetry. AFMTC-TR-57-22, U.S. Air Force, Aug. 1957. (Available from DDC as AD 124 144.)

6. Sweer, John: The Path of a Ray of Light Tangent to the Surface of the Earth. J. Opt. Soc. America, vol. 28, no. 9, Sept. 1938, pp. 327-329.

7. Smart, W. M.: Text-Book on Spherical Astronomy. Cambridge Univ. Press, 1956.

8. Snider, Donald E.: Refractive Effects in Remote Sensing of the Atmosphere With Infrared Transmission Spectroscopy. J. Atmos. Sci., vol. 32, no. 11, Nov. 1975, pp. 2178-2184.

9. Eisenhart, Luther Pfahler: Coordinate Geometry. Ginn and Co., c.1939.

TABLE I.- TIMING OVERLAP BETWEEN CAMERAS

| Payload | | | |
|---|---|---|---|
| Station 438 | Plate 121217 | Station 432 | Plate 121224 |
| Time,[a] s | | Time,[a] s | |
| 448.91 | | | |
| 449.43 | | | |
| 449.96 | | | |
| 450.49 | | | |
| 451.02 | | | |
| 451.52 | | | |
| 452.08 | | | |
| 452.63 | | | |
| 453.13 | | | |
| 454.18 | | | |
| 454.70 | | | |
| 455.97 | | | |
| 456.29 | | | |
| - - - - - - - - - - - - - - - - | | - - - - - - - - | 456.58 - - - - |
| | | | 457.10 |
| 457.34 | | | |
| | | | 457.73 Effective overlap |
| 457.88 | | | |
| | | | 458.27 |
| 458.40 | | | |
| | | | 458.79 |
| 458.93 - - - - - - - - - - | | - - - - - - - - - - - - - - - - | |
| | | | 459.30 |
| | | | 460.27 |

[a]Time is seconds from launch; read at end of each exposure.

TABLE II.- COMPUTED TARGET DATA

| Range time, s | Height, km | Latitude north | Longitude west |
|---|---|---|---|
| 457.8 | 20.283 | 33.2402 | -62.9741 |
| 458.0 | 19.871 | 33.2353 | -62.9635 |
| 458.2 | 19.437 | 33.2312 | -62.9528 |
| 458.4 | 19.010 | 33.2253 | -62.9422 |
| 458.6 | 18.591 | 33.2197 | -62.9313 |

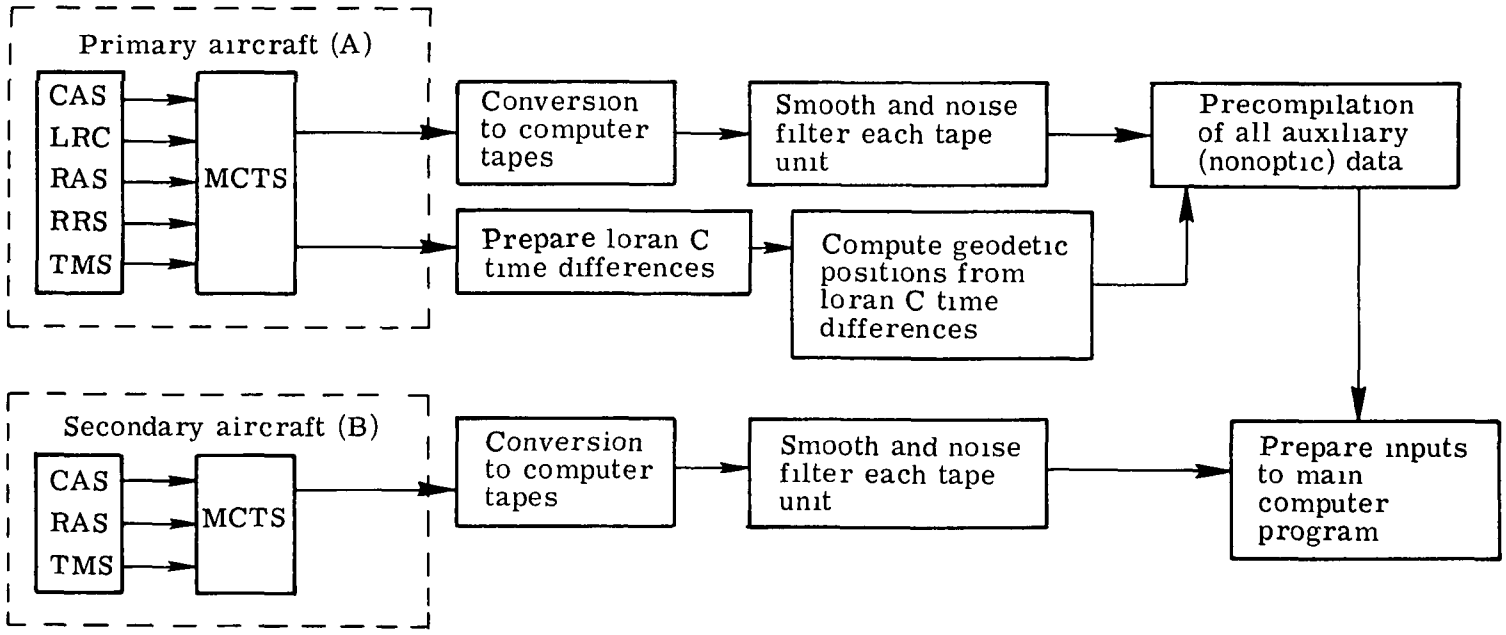


CAS Ballistic camera system (shutter timing)
LRC Loran C time difference system
MCTS Multichannel tape system
RAS Radar altimeter system
RRS Radar ranging system
TMS Timing mechanism system

Figure 1.- Auxiliary data processing.

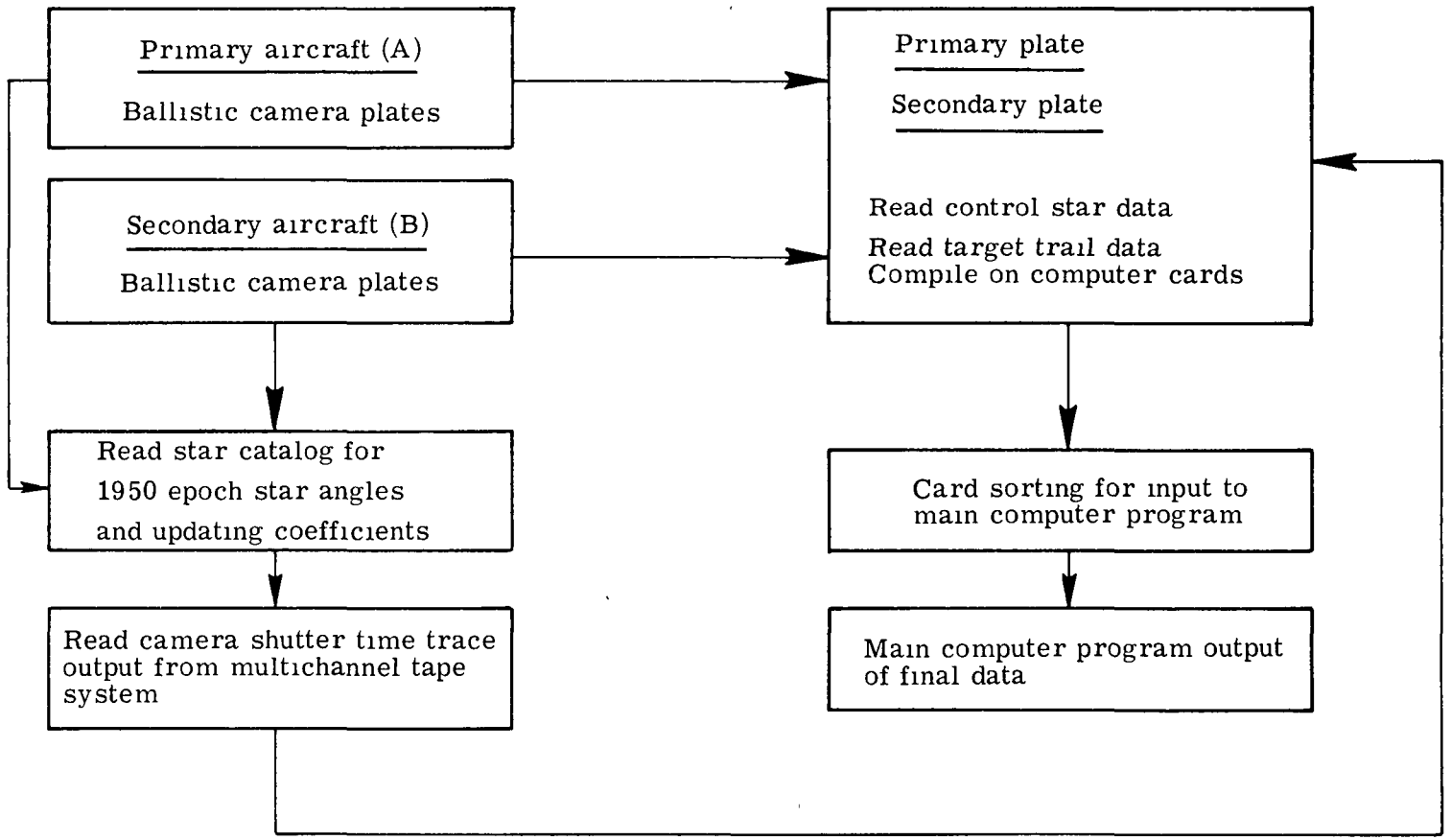


Figure 2.- Camera-plate data processing.

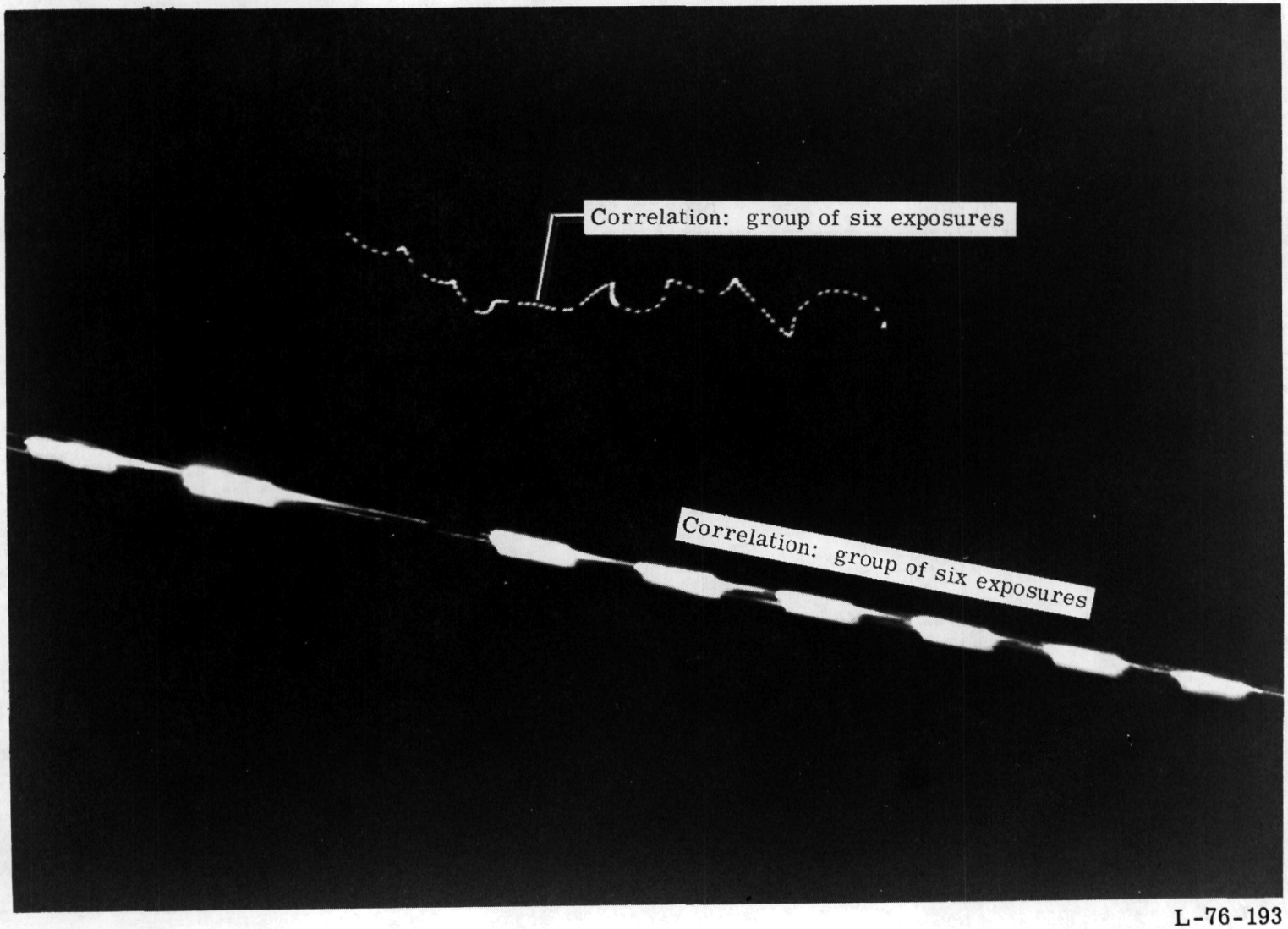


L-76-193

Figure 3.- Enlargement section, plate 121216, aircraft 432.

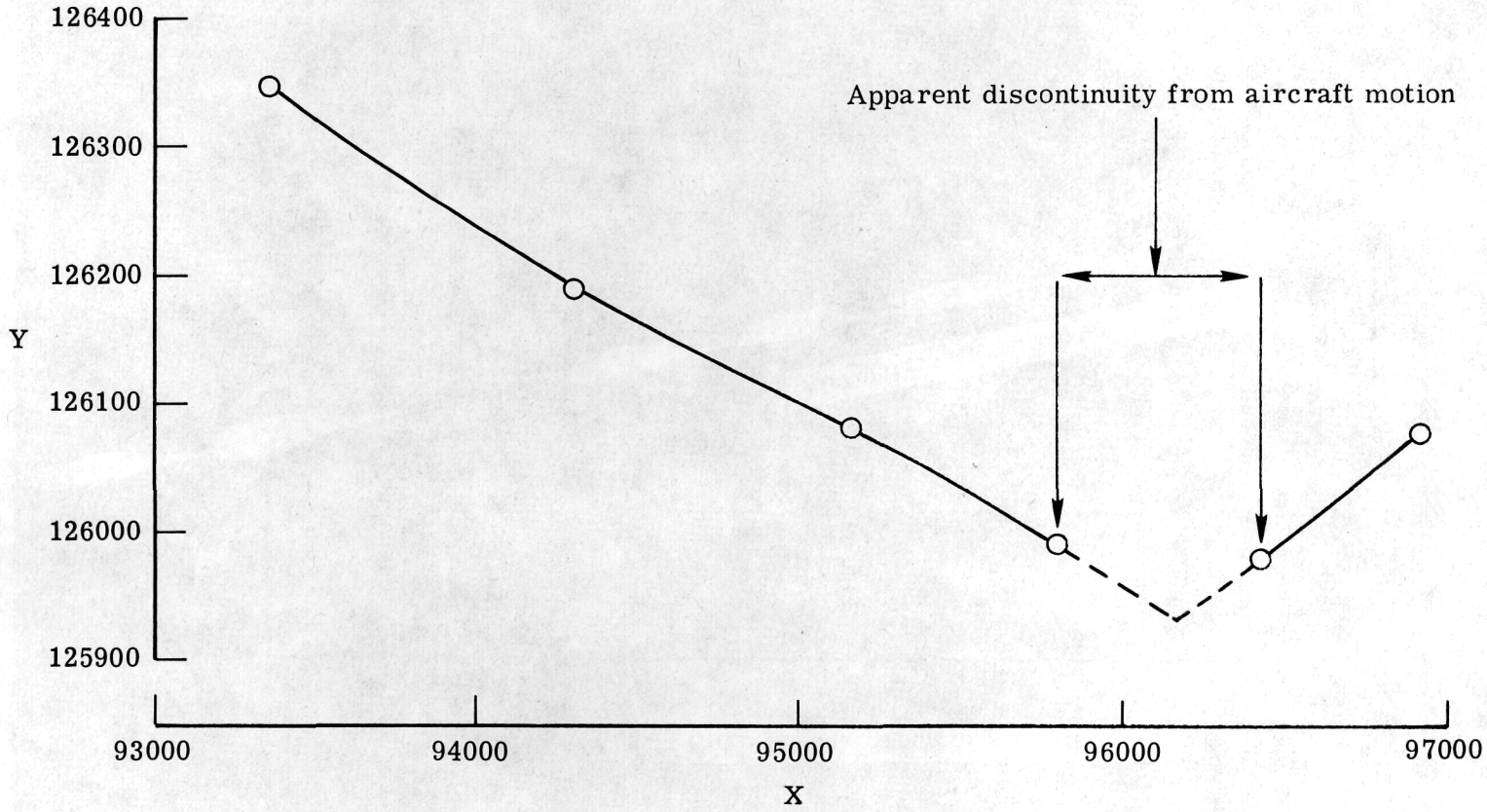


Figure 4.- Plate 121216, star No. 11593, XY-plate reading ($\mu$m).

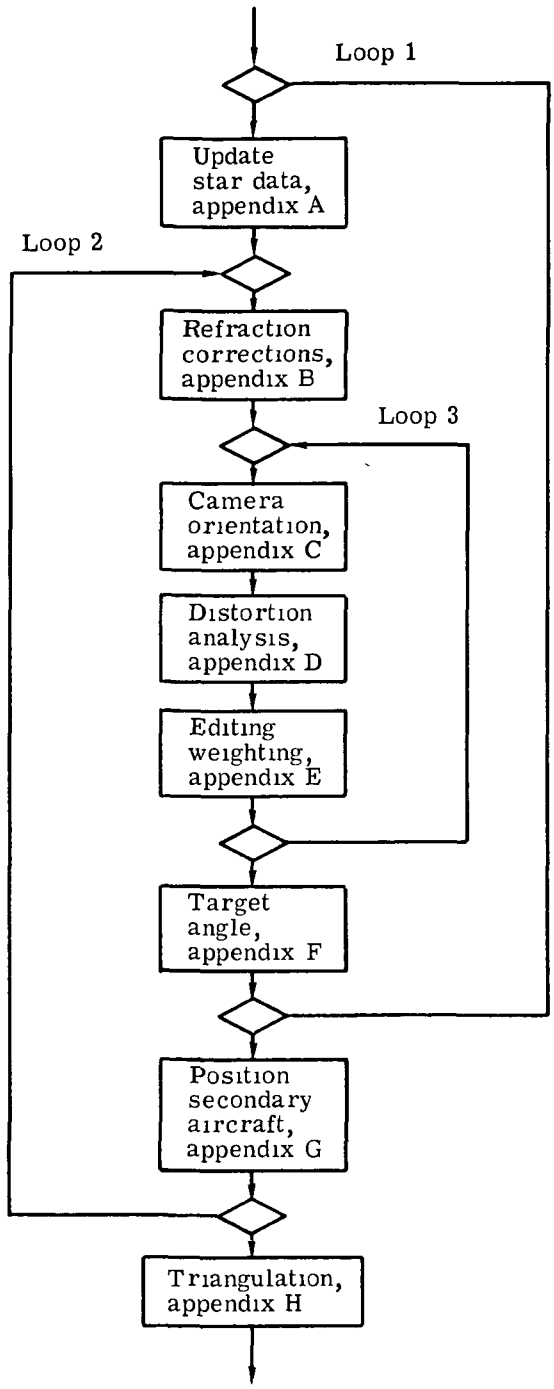


Figure 5.- Data-reduction sequence.

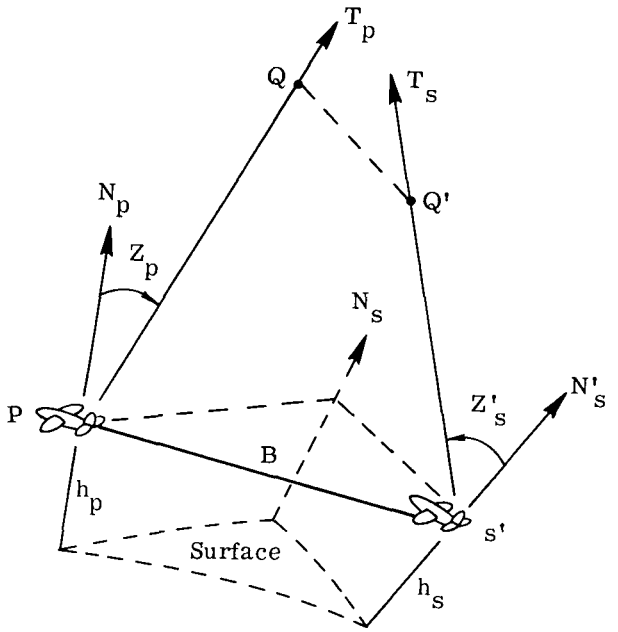


(a) Navigator's estimate, secondary aircraft position.

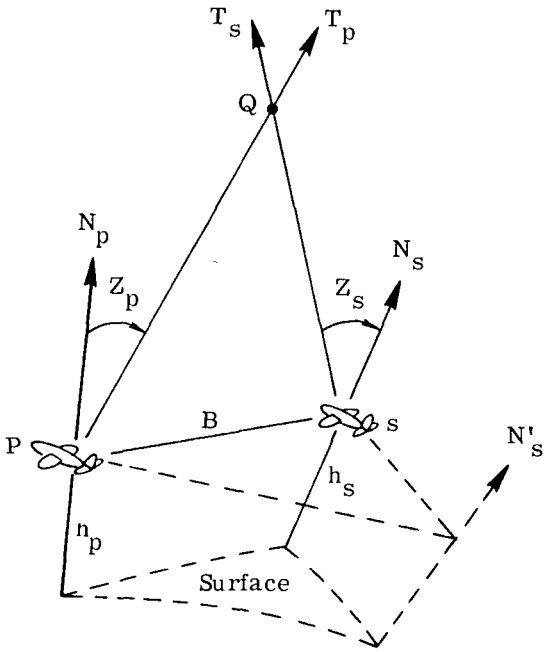


(b) Adjusted secondary aircraft position.

Figure 6.- Secondary aircraft positions.

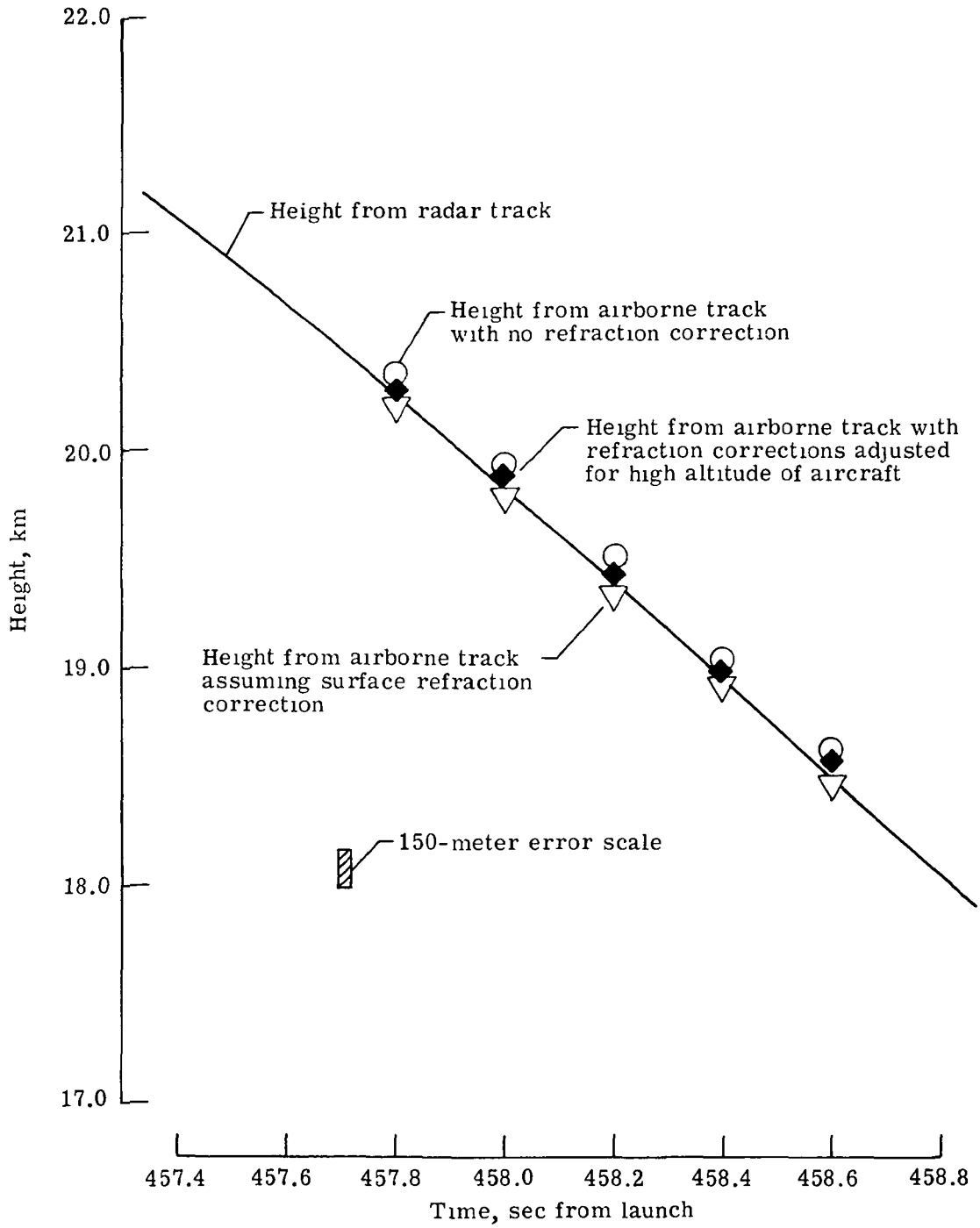


Figure 7.- Time-height profile.

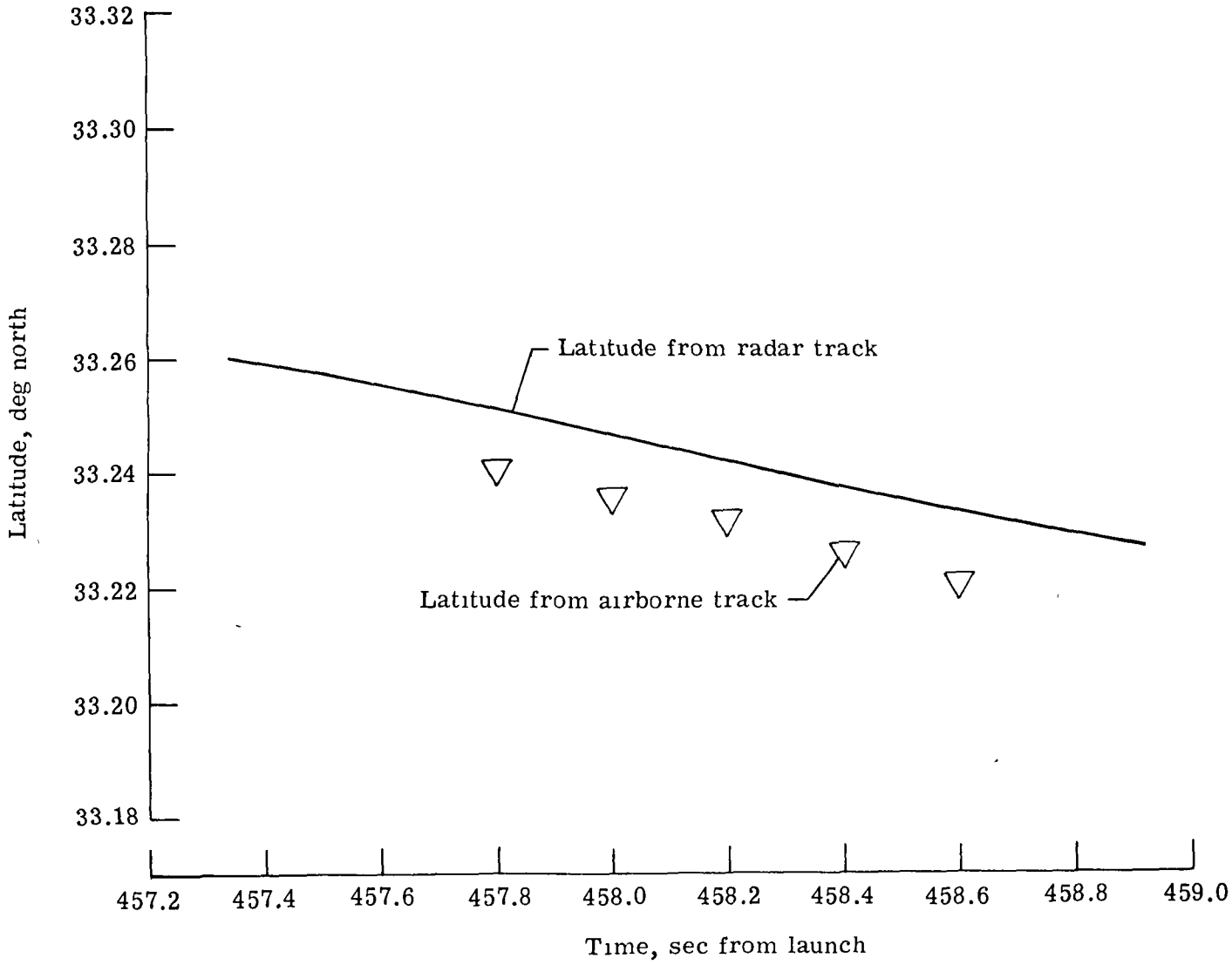


Figure 8.- Time-latitude profile.

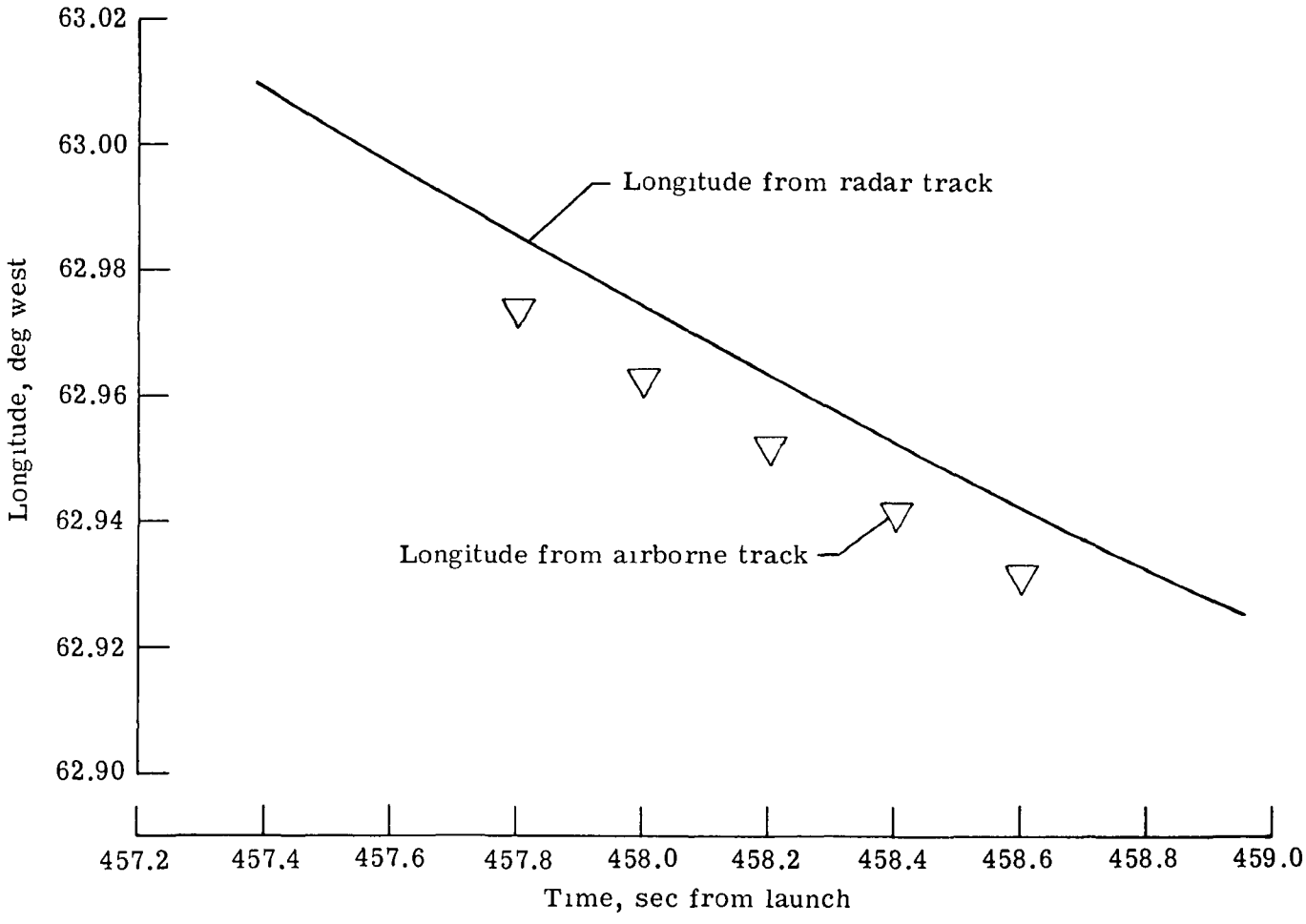


Figure 9.- Time-longitude profile.

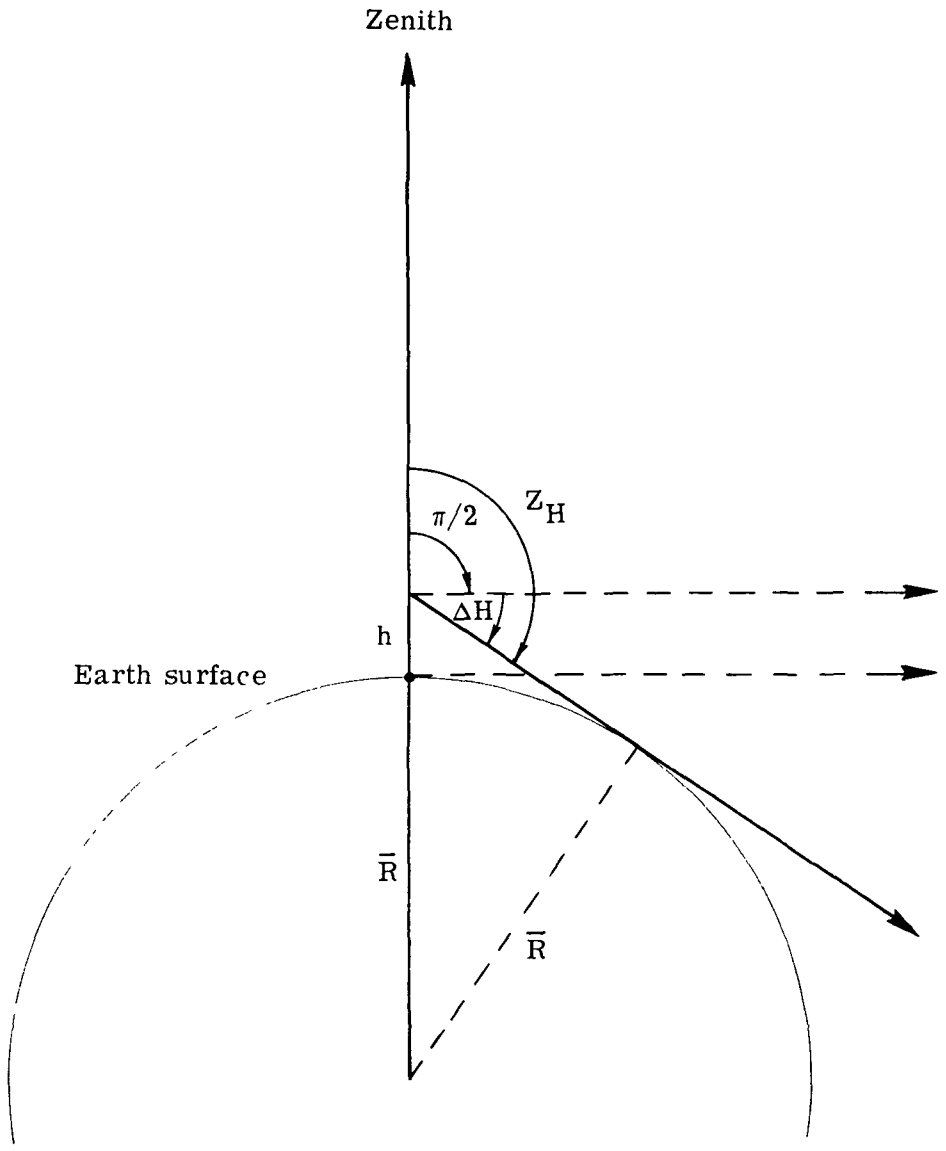


Figure 10.- Scaled zenith angle.

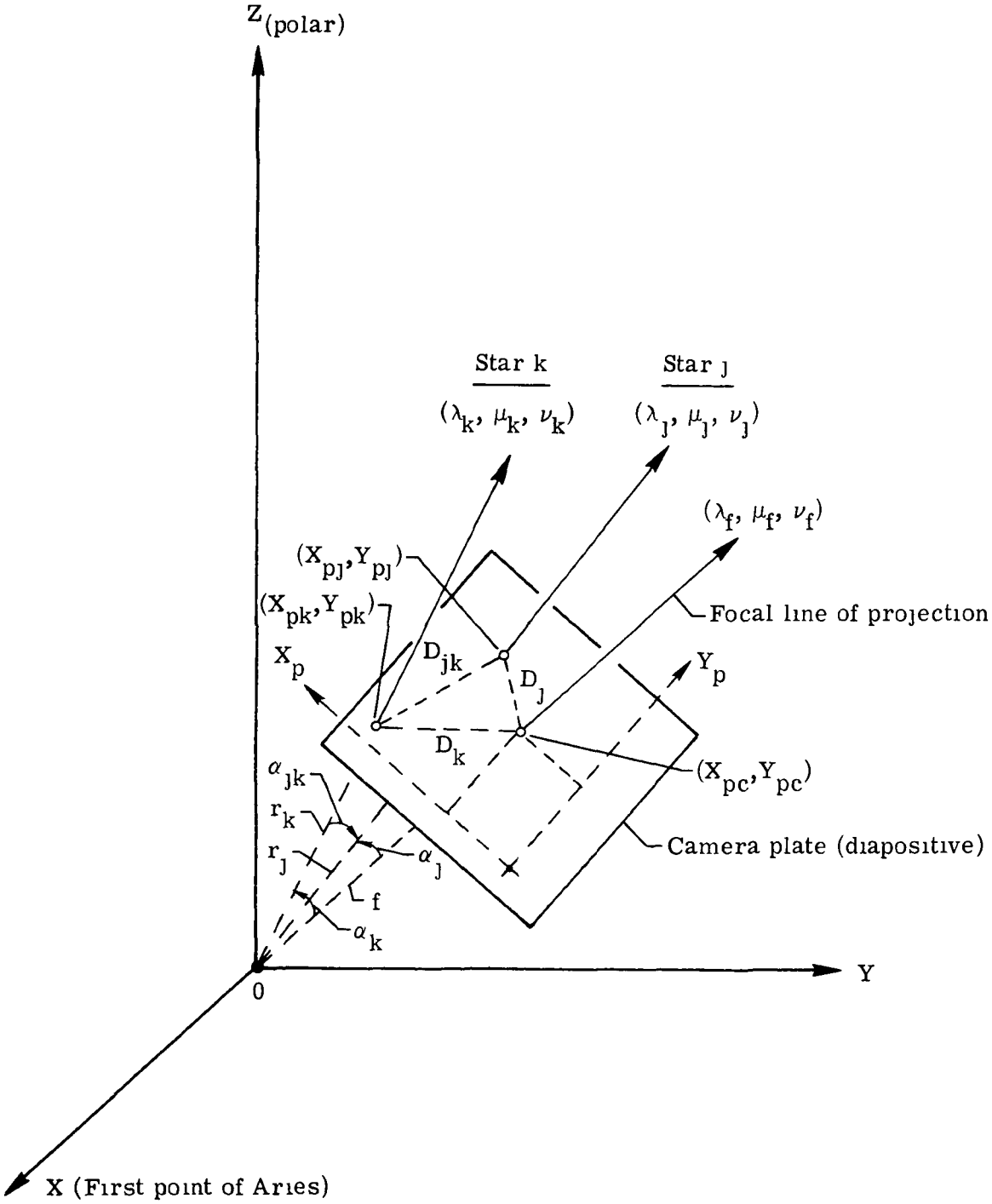


Figure 11.- Camera plate displacement geometry.

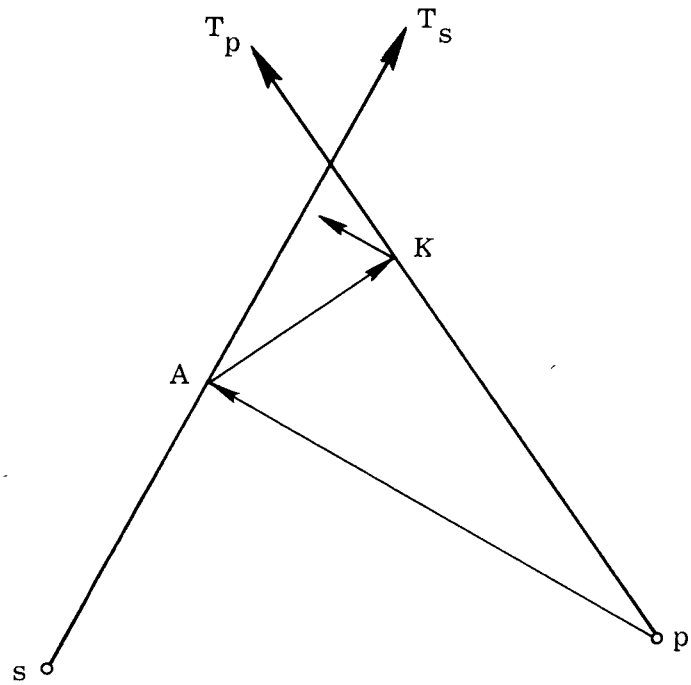


Figure 12.- Triangulation procedure.

*"The aeronautical and space activities of the United States shall be conducted so as to contribute . . to the expansion of human knowledge of phenomena in the atmosphere and space. The Administration shall provide for the widest practicable and appropriate dissemination of information concerning its activities and the results thereof."*

—NATIONAL AERONAUTICS AND SPACE ACT OF 1958

# NASA SCIENTIFIC AND TECHNICAL PUBLICATIONS

TECHNICAL REPORTS Scientific and technical information considered important, complete, and a lasting contribution to existing knowledge.

TECHNICAL NOTES Information less broad in scope but nevertheless of importance as a contribution to existing knowledge

TECHNICAL MEMORANDUMS Information receiving limited distribution because of preliminary data, security classification, or other reasons Also includes conference proceedings with either limited or unlimited distribution.

CONTRACTOR REPORTS Scientific and technical information generated under a NASA contract or grant and considered an important contribution to existing knowledge

TECHNICAL TRANSLATIONS Information published in a foreign language considered to merit NASA distribution in English

SPECIAL PUBLICATIONS Information derived from or of value to NASA activities Publications include final reports of major projects, monographs, data compilations, handbooks, sourcebooks, and special bibliographies.

TECHNOLOGY UTILIZATION PUBLICATIONS Information on technology used by NASA that may be of particular interest in commercial and other non-aerospace applications. Publications include Tech Briefs, Technology Utilization Reports and Technology Surveys.

***Details on the availability of these publications may be obtained from:***

**SCIENTIFIC AND TECHNICAL INFORMATION OFFICE**

**NATIONAL AERONAUTICS AND SPACE ADMINISTRATION**

**Washington, D.C. 20546**